

# Magnetic metastability driven Anomalous Hall Effect in $\text{Fe}_x\text{TaS}_2$

Mohamad Numan<sup>1</sup>, Prasanta Chowdhury<sup>1</sup>, Sanat Adhikary<sup>2</sup>, Saurav Giri<sup>1</sup>, Jhuma Sannigrahi<sup>3</sup>, Matthias Gutmann<sup>4</sup>, Souvik Chatterjee<sup>2</sup>, and Subham Majumdar<sup>1\*</sup>

<sup>1</sup>*School of Physical Science, Indian Association for the Cultivation of Science, 2A & B Raja S. C. Mullick Road, Jadavpur, Kolkata 700 032, INDIA*

<sup>2</sup>*UGC-DAE Consortium for Scientific Research, Kolkata Centre, Sector III, LB-8, Salt Lake, Kolkata 700 106, India*

<sup>3</sup>*School of Physical Sciences, Indian Institute of Technology Goa, Farmagudi, Goa 403401, India and*

<sup>4</sup>*ISIS Neutron and Muon Source, Science and Technology Facilities Council, Rutherford Appleton Laboratory, Chilton Didcot OX11 0QX, United Kingdom*

We have investigated the magnetic and transport properties of Fe-intercalated TaS<sub>2</sub> single crystals. The material exhibits ferromagnetic order with very high anisotropy, with the *c*-axis as the easy axis. The magnetic moments of the compound become arrested during field cooling in magnetic fields above 500 Oe. As a result, it retains thermoremanent magnetization (TRM) up to the transition temperature ( $T_C$ ).  $\text{Fe}_x\text{TaS}_2$  displays a large anomalous Hall effect (AHE) with a pronounced hysteresis loop, similar to the isothermal magnetization. Our key observation suggests that the presence of TRM breaks the time-reversal symmetry below  $T_C$ , producing an AHE in zero applied field with the same value as that obtained from typical field variation. Scaling analysis indicates that skew scattering is the primary mechanism for the observed AHE.

## I. INTRODUCTION

Layered van der Waals (vdW) materials continue to garner significant attention due to their fascinating physical properties, both from a fundamental physics perspective and for their potential applications in various two-dimensional (2D) spintronics devices [1–3]. Among them, transition metal dichalcogenides with general formula  $\text{TX}_2$  ( $T = 4d$  or  $5d$  transition metal, and  $X =$  chalcogen) are of particular interest due to their fascinating electronic, optical, and mechanical properties. In terms of electronic properties,  $\text{TX}_2$  exhibits various body phenomena, including superconductivity [4], charge density wave (CDW) instabilities [5–7], and even a quantum spin liquid state [8–10].

The quasi 2D structure of  $\text{TX}_2$  enables us to intercalate various metal atoms in the vdW gap between two  $\text{TX}_2$  layers. Very recently,  $3d$  metal intercalated  $\text{TX}_2$  compounds emerged as a test bed for studying topological effects related to magnetism, which include chiral magnetic soliton lattice arising from chiral helimagnetic structure [11] and a giant planar Hall effect in  $\text{Cr}_{1/3}\text{NbS}_2$  [12], as well as a spontaneous topological Hall effect induced by non-coplanar antiferromagnetic order in  $\text{Co}_{1/3}\text{NbS}_2$  and  $\text{Co}_{1/3}\text{TaS}_2$  [13]. The long-range order and structural properties of these intercalated materials strongly depend on the specific TM and the percentage of intercalation ( $x$ ) [14–16].

Among the various intercalated  $\text{TX}_2$ , Fe-intercalated TaS<sub>2</sub> displays unique magnetic properties. For intercalation levels  $0.23 \leq x \leq 0.4$ , the material exhibits ferromagnetic (FM) order. In particular, the Curie point ( $T_C$ ) increases as  $x$  decreases, although no perfect correlation

has been identified, as  $T_C$  continues to rise even with further reductions in  $x$  [17]. At specific intercalation levels, such as  $x = 1/4$  or  $x = 1/3$ , the intercalated Fe ions arrange themselves into a superlattice. This superlattice exhibits periodic arrangements, forming  $2a \times 2a$  or  $\sqrt{3}a \times \sqrt{3}a$  superstructures, respectively.

In recent times, there has been a growing interest in understanding the anomalous Hall effect (AHE), and these  $3d$  metal intercalated materials provide an excellent platform for exploring their electronic states. Despite numerous studies, one report rigorously addresses AHE in  $\text{Fe}_{1/4}\text{TaS}_2$ , demonstrating that the intrinsic mechanism, driven by the Berry phase, is responsible for the observed AHE below 50 K [18].

We have prepared single crystals of  $\text{Fe}_x\text{TaS}_2$  ( $x \sim 0.27$ ) and investigated the significant metastability in the system. This manifests itself as domain locking during field cooling with a field as small as 500 Oe. This metastable state persists up to  $T_C$ , keeping the system magnetically trapped under weak field cooling.

Importantly, this metastability spontaneously breaks the time-reversal symmetry at low temperatures, producing a robust AHE without any external field. Scaling analysis identifies skew scattering as the primary mechanism for the observed AHE, which is comparable in magnitude to that induced by external fields. These findings highlight the critical role of metastability in driving the electronic and magnetic properties of  $\text{Fe}_x\text{TaS}_2$ .

## II. EXPERIMENTAL METHODS

Single crystals of  $\text{Fe}_x\text{TaS}_2$  were synthesized using the standard chemical vapor transport method, with iodine as transport agent. The resulting crystals exhibit a flat plate-shaped geometry along the *ab* plane, as shown in the inset of Fig. 1 (a), with typical dimensions in the

\* sspsm2@iacs.res.in

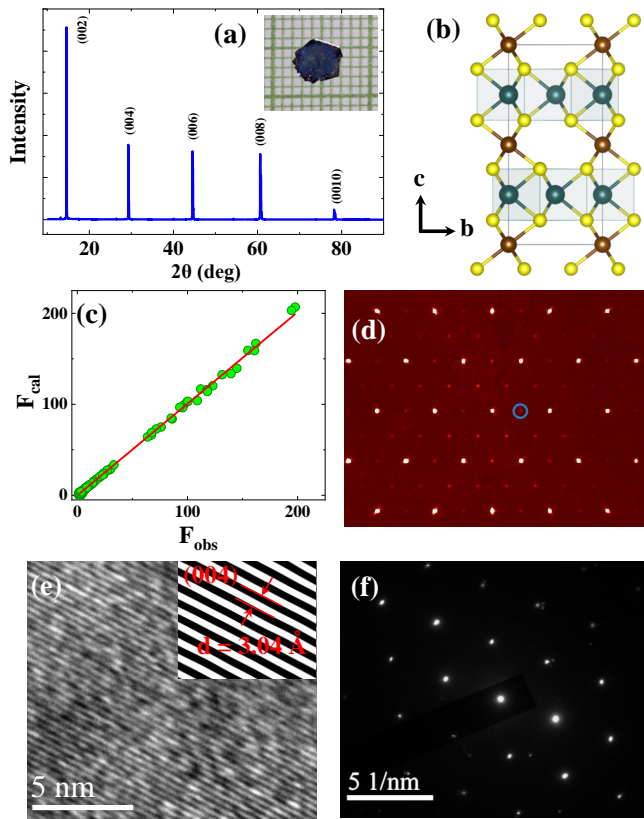


FIG. 1. (a) XRD pattern in the flat surface of the crystal, showing sharp peaks corresponding to  $(0\ 0\ 2l)$  reflections, confirming its highly oriented layered structure. The inset displays an optical image of the sample crystal placed on to a  $1\text{ mm} \times 1\text{ mm}$  graph paper. (b) Crystal structure schematic of the material, highlighting the layered arrangement with the Fe atoms (brown colored) intercalated in between van der Waals gaps. (c) Observed versus calculated structure factors ( $F_{\text{obs}}$  vs.  $F_{\text{cal}}$ ), confirming the reliability of the structural refinement. (d) Single crystal x-ray diffraction pattern confirming the crystallinity of the sample with distinct diffraction spots in the  $ab$  plane of the reciprocal space. (e) HRTEM image showing lattice fringes with an interplanar spacing of  $3.04\text{ \AA}$ , as shown in the inset. (f) Selected area electron diffraction (SAED) pattern, with a marked spot corresponding to a specific reflection.

millimeter range. The crystal structure and phase purity were verified by x-ray diffraction (XRD) and single-crystal x-ray diffraction (SCXRD). XRD on the flat plane  $ab$  was performed using a RIGAKU SmartLab system (4.5 kW) with  $\text{Cu } K_{\alpha}$  radiation (wavelength  $\lambda = 1.5406\text{ \AA}$ ). SCXRD data were collected using a Rigaku-Oxford Diffraction Xtalab Synergy single-crystal diffractometer equipped with a HyPix hybrid pixel array detector and  $\text{Mo } K_{\alpha}$  radiation. Data reduction, structure solution, and refinement were performed using CrysAlisPRO, SHELXT [19], and JANA2020 [20] software respectively.

The stoichiometry of the compound was confirmed by energy-dispersive x-ray (EDX) analysis using a JEOL JSM-6010LA scanning electron microscope (SEM). High-

resolution transmission electron microscopy (HRTEM) and selected area electron diffraction (SAED) were conducted with a JEOL TEM 2010. Magnetic measurements were performed using a Quantum Design Magnetic Properties Measurement System (MPMS3). Electrical transport measurements ( $\rho_{xx}$  and  $\rho_{yx}$ ) were performed with a cryogen-free high magnetic field system from Cryogenic Ltd., UK.

TABLE I. Crystallographic and Structural Parameters for  $\text{Fe}_x\text{TaS}_2$

Category	Parameter	Value			
Crystal System	Crystal System	Hexagonal			
	Space Group	$P6_3/mmc$			
	Unit Cell	$a = 6.62432(15)\text{ \AA}$			
	Dimensions	$c = 12.1878(4)\text{ \AA}$			
	Unit Cell Volume	$V = 463.17(2)\text{ \AA}^3$			
	Z	8			
Experimental Details	Density (cal)	$7.4293\text{ g/cm}^3$			
	Radiation	$\text{Mo } K_{\alpha}, \lambda = 0.71073\text{ \AA}$			
	Temperature	295 K			
	$2\theta$ Range	$3.35^\circ$ to $65.32^\circ$			
	Refl. Collected	10303			
	Ind. Reflections	357			
Atomic Parameters	G.O.F.	1.97			
	R Index for all data	$R_1 = 0.0358$ $wR_2 = 0.069$			
	Atom Positions	See below			
	$(x, y, z)$ and $U_{\text{ani}}$	See below			
	Atom	x	y	z	$U_{\text{ani}} (\text{\AA}^2)$
	Ta1	0.49701(2)	0.50299(2)	3/4	0.0069(3)
Ta2	0	0	0	0.005(3)	
Fe	0	0	0	0.031(3)	
S1	2/3	1/3	0.12006(13)	0.0063(5)	
S2	0.83252(8)	0.16748(8)	0.62198(10)	0.006(4)	

### III. RESULTS

#### A. Structural and Phase Analysis

The SCXRD data at room temperature show that  $\text{Fe}_x\text{TaS}_2$  forms a hexagonal crystal structure with the  $P6_3/mmc$  space group. The linear correlation between the observed ( $F_{\text{obs}}$ ) and calculated ( $F_{\text{cal}}$ ) structure factors, shown in Fig. 1(c), indicates satisfactory structural refinement. The refined crystallographic and statistical parameters are listed in Table I.

The XRD pattern, obtained in the Bragg-Brentano  $\theta$ - $\theta$  geometry on the flat surface of the crystal [see Fig. 1 (a)], displays peaks corresponding to the  $(0\ 0\ 2l)$  planes, confirming that the flat surface represents the  $ab$  plane. Fig. 1(b) illustrates the arrangement of Fe atoms (brown), which are intercalated in the vdW gaps between

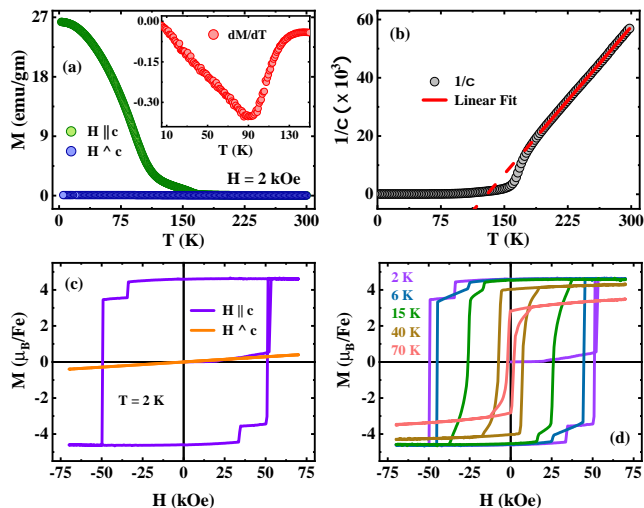


FIG. 2. (a) Temperature-dependent magnetization ( $M$ - $T$ ) measured in field-cooled (FC) protocol under an applied field of 2 kOe with  $H \parallel c$  and  $H \perp c$  configurations. The inset shows the  $dM/dT$  plot with  $T$  under  $H = 2$  kOe, when  $H \parallel c$ . (b) The inverse susceptibility ( $1/\chi$ ) as a function of  $T$ . The red line displays linear fit to the data. (c) Isothermal magnetization ( $M$ - $H$ ) loop at 2 K for  $H \parallel c$  and  $H \perp c$  configurations, highlighting magnetic anisotropy along  $c$  axis. (d) Temperature-dependent  $M$ - $H$  loops at selected temperatures (2 K, 6 K, 15 K, 40 K, and 70 K), showing the evolution of magnetic hysteresis with  $T$ .

TaS<sub>2</sub> layers, forming a triangular network in the  $ab$  plane. Additionally, the SCXRD pattern [Fig. 1(d)] reveals less intense spots, marked with blue circles, which correspond to  $2a \times 2a$  superstructures previously reported in the literature.

The SEM energy-dispersive spectra confirm a compositional ratio of Fe : Ta : S = 0.269 : 1 : 1.98, indicating Fe content close to 0.25, consistent with the crystal structure derived from SCXRD. The HRTEM image in Fig. 1(e) shows an interplanar spacing of 3.04 Å for the (0 0 4) planes. The layered morphology and crystalline nature of Fe<sub>x</sub>TaS<sub>2</sub> are further verified by SAED patterns, as shown in Fig. 1(f). The lattice parameters obtained from SAED and XRD are in close agreement with each other.

## B. Magnetization

Figure 2 (a) presents the temperature ( $T$ ) dependence of magnetization ( $M$ ) under field-cooled (FC) protocol at an applied field of 2 kOe along the  $c$  axis (green symbols) and perpendicular to the  $c$  axis (blue symbols). As the temperature decreases from 300 K,  $M$  initially increases slowly. Below approximately 160 K, FC  $M$  rises rapidly, with a sharper increase observed below about 100 K for  $H \parallel c$ . In contrast, when  $H \perp c$ , the value of  $M$  is significantly lower, more than two orders of magnitude

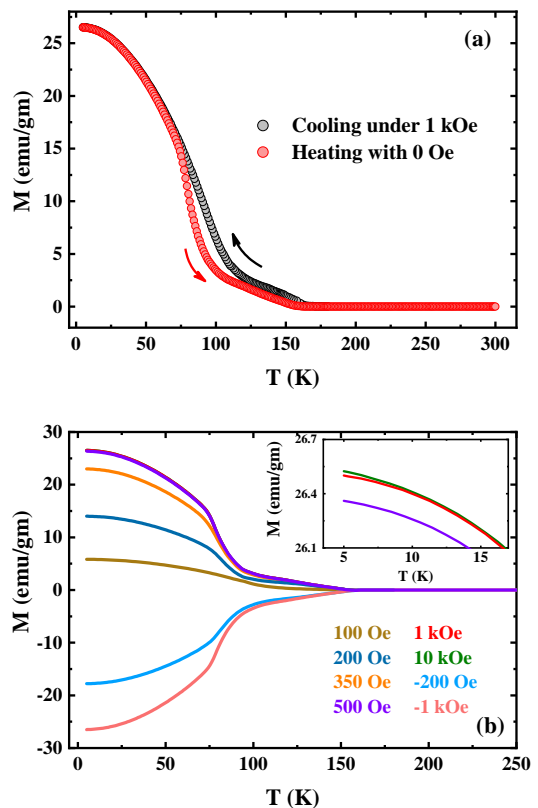


FIG. 3. (a)  $T$  dependent magnetization measured during cooling from 300 K under  $H_{cool} = 500$  Oe (black circles) and subsequent heating to 300 K in zero-field (red circles). The arrows indicate the direction of  $T$  change. (b)  $M$ - $T$  curves measured during heating in zero-field after field cooling under various positive and negative cooling fields, demonstrating the thermoremanent magnetization. The inset highlights the low-temperature region, showing subtle variations in  $M$  for  $H_{cool} \geq 500$  Oe.

lower, indicating a strong anisotropy in the system. The inset of Fig. 2(a) shows the first derivative of  $M$  with respect to  $T$ , which exhibits a dip around 90 K, marking the long-range ordering temperature,  $T_C$  of the system.

Figure 2(b) shows the linear fit to the inverse susceptibility ( $1/\chi$ , where  $\chi = M/H$ ), revealing a ferromagnetic ground state with a Curie-Weiss temperature of  $\theta = 129$  K. The data deviates significantly from linearity below 200 K, likely due to the presence of short-range correlations in the system.

The isothermal magnetization curves at 2 K, with  $H$  applied along and perpendicular to the  $c$  axis, are shown in Fig. 2 (c). For  $H \parallel c$ ,  $M$  initially increases linearly with  $H$ . However, above 50 kOe,  $M$  increases sharply and subsequently saturates above 52 kOe with saturation moment  $M_s = 4.6 \mu_B/\text{Fe}$ . Upon decreasing the magnetic field, a high remnant magnetization is observed and  $M$  turns sharply negative when the field exceeds  $-49$  kOe. A large hysteresis loop is evident, with a coercivity of about 50 kOe. In contrast, for  $H \perp c$ , the  $M$ - $H$  curve remains linear and shows no sign of saturation even up to

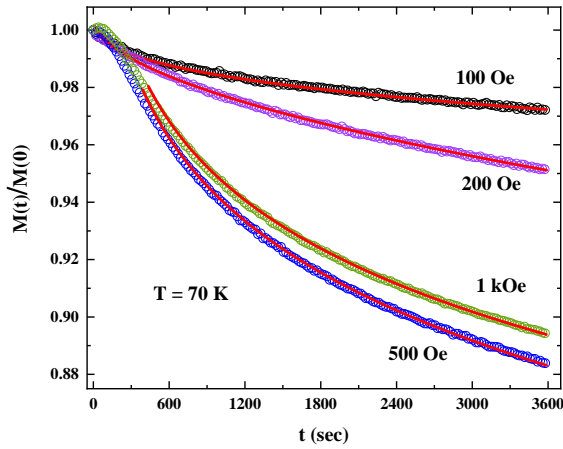


FIG. 4. (a) Normalized relaxation  $M(t)/M(0)$  as a function of time at 70 K. The measurement was performed by cooling the sample to 70 K from 200 K followed by recording the relaxation over the course of an hour after the removal of applied field.

80 kOe. In particular, the magnetization in this direction is significantly smaller compared to  $H \parallel c$ . This confirms the strong anisotropy in the material, with the  $c$  axis being the easy axis and the  $ab$  plane acting as the hard plane.

Fig. 2 (d) shows several  $M$ - $H$  isotherms recorded at different temperatures. As  $T$  is increased the coercivity of the sample decreases and it attains a value as low as 8 kOe at 70 K. The value of  $M_s$  also decreases with increasing  $T$ .

The presence of a square  $M$ - $H$  loop and remanent magnetization ( $M_R$ ) with large coercivity likely reflects the significant magnetic anisotropy and the Ising nature of the spins [21]. Notably, the value of  $M_R$  remains substantial even at higher temperatures. This highlights the importance of investigating the evolution of remanent magnetization as a function of temperature, which is generally referred to as thermoremanent magnetization (TRM) [22–25]. The sample is cooled in an applied magnetic field below a characteristic temperature  $T_0$ , which may be the spin freezing temperature for the spin glass or the magnetic ordering temperature for the long-range ordered system. The magnetic field is then removed and  $M^{tr}$  is measured as a function of temperature. To investigate the TRM for  $\text{Fe}_x\text{TaS}_2$ , we cooled the sample to 3 K from much above  $T_c$  under various cooling fields ( $H_{cool}$ ), and in each case, the sample was subsequently heated after removal of  $H_{cool}$  [see Fig. 3]. We observe that even in zero-field, a significant  $M^{tr}$  is present, even for  $H_{cool} = 100$  Oe. We found that as  $H_{cool}$  increases,  $M^{tr}$  increases for  $H_{cool}$ , and for  $H_{cool} \geq 500$  Oe,  $M^{tr}$  reaches saturation. To further confirm TRM in the compound studied, we cooled the sample in negative  $H_{cool}$  (-200 Oe and -1 kOe), which provides negative  $M^{tr}$  signifying sign reversal under  $H_{cool}$ . It should be noted that for both negative and positive  $H_{cool}$ ,  $M^{tr}$  vanished for  $T > 160$  K.

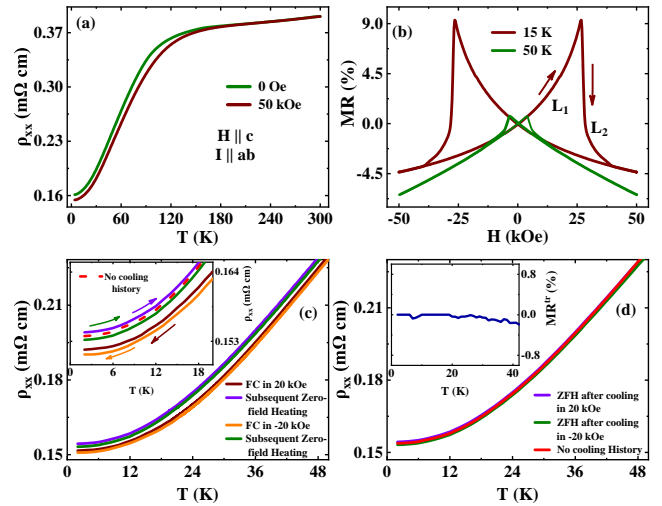


FIG. 5. (a) Temperature variation of the longitudinal resistivity under zero applied field (green) and 50 kOe (wine) are displayed. Both datasets were recorded while cooling the sample from 300 K. (b) shows the field variation of percentage MR at  $T = 15, 50$  and 100 K. (c) Longitudinal resistivity during FC from 300 K to 2 K in 20 kOe and subsequent heating from 300 K to 2 K in zero-field. The same protocol was also repeated in -20 kOe and zero-field. Inset shows the magnified view of this at low  $T$ , the arrow represents the direction of  $T$  change. (d) Here only the zero-field heating curves are plotted, two are from FC procedure in  $\pm 20$  kOe and red line without any FC history. Inset displays the MR obtained after symmetrization due to the TRM at low  $T$ .

Considering the irreversible nature of  $M$ , it is pertinent to study the time evolution of remanent magnetization in the FC state. In this process, the sample was cooled from 200 K under an applied field of  $H_{cool} = 500$  Oe to a suitable temperature ( $T_{rlx}$ ) for relaxation measurement. Subsequently, the field is removed and  $M$  was measured as a function of time ( $t$ ). We perform relaxation measurements for several values of  $T_{rlx}$ , namely 10, 25, 70 K, for an hour. Interestingly, the data at 10 K and 25 K show an insignificant relaxation (around 1%) over the course of one hour (Fig. 4). In contrast, the data at 70 K show a large relaxation (more than 10%), as shown in Fig. 4.

To further investigate this, relaxation was measured for different values of  $H_{cool}$  at  $T_{rlx} = 70$  K. The data for  $H_{cool} = 100$  and 200 Oe exhibit typical relaxation obeying stretched exponential [ $\sim e^{-(t/\tau)^\beta}$ ] behavior. Here,  $\tau$  is the time constant for relaxation and  $\beta$  is the stretching exponent. However, the normalized relaxations at 500 Oe and 1 kOe show different behavior compared to low-field data. Interestingly, the stretched exponential function cannot fit the full range data for  $H_{cool} \geq 500$  Oe. This deviation can be traced back to the fact that field cooling in  $H_{cool} \geq 500$  Oe produces a fully saturated magnetically arrested state, which is not achieved for  $H_{cool} = 100$  or 200 Oe. However, for  $H_{cool} \geq 500$  Oe, the stretched exponential function can adequately fit the data after the

initial 500 seconds of relaxation.

### C. Magneto-transport and Hall effect

The temperature dependence of longitudinal resistivity ( $\rho_{xx}$ ) in zero-field (blue line) and under an applied field of 50 kOe (orange line), within the  $T$  range of 3 to 300 K, is presented in Fig. 5 (a). Measurements were carried out with the current applied in the  $ab$  plane and  $H$  along the  $c$  axis for the 50 kOe data. The data were recorded while cooling from 300 K. In zero-field, the resistivity ( $\rho_{xx}$ ) shows an almost linear dependence on  $T$  above 150 K, below which it falls rapidly showing typical metallic behavior. Under  $H = 50$  kOe,  $\rho_{xx}$  shifts downward, indicating negative magnetoresistance (MR). This behavior is consistent with the reduction of spin-disorder scattering of electrons under an applied magnetic field.

Furthermore, the field variation of MR at  $T = 15$  and 50 is shown in Fig. 5 (b) for  $H$  applied along the  $c$ -axis. At  $T = 15$  K, MR increases with  $H$ . However, with further increases in  $H$ , MR drops sharply to a negative value within a very narrow range of  $H$  and then decreases linearly as  $H$  increases further. When  $H$  is reversed, a similar behavior is observed, resulting in a bow-tie shape-type hysteresis loop, as previously reported [26]. In particular, as  $T$  increases, the width of the bow-tie loop becomes narrower, and the MR becomes more linear. One can notice that the sharp drop in MR [L<sub>2</sub>, see 15 K data of Fig. 5(b)] correspond to the coercive field of  $M$ - $H$  and  $\rho_{yx}$ - $H$  data. The loop L<sub>1</sub> is obtained after saturating the sample in negative field and then increasing the field in the positive quadrant. Here the positive transverse-MR occurs due to the bending of the electron trajectory. Eventually, the spin gets aligned to the positive field direction at the coercive field (here about 25 kOe for the 15 K data), and  $\rho_{xx}$  drops due to coherent scattering of the charge carriers and the spin moments.

Since Fe<sub>x</sub>TaS<sub>2</sub> exhibits a large TRM with  $H_{cool}$  as low as 500 Oe, it is important to understand the effect of TRM on MR. To investigate this,  $\rho_{xx}$  was measured during the cooling of the sample from 300 K to 2 K under  $H_{cool} = 20$  kOe, as shown by the wine-colored line in Fig. 5 (c). After that, the field was removed and  $\rho_{xx}$  was measured again (purple line) while heating. Upon removal of  $H_{cool}$  at 2 K,  $\rho_{xx}$  jumps back to the simple zero-field cooling resistivity curve ( $\rho_{xx}^0$ ), and follows the curve throughout the temperature range. Here, the curve  $\rho_{xx}^0$  is obtained by heating the sample in  $H = 0$  after cooling down to 2 K in zero-field. The same protocol was followed for  $H = -20$  kOe, as shown by the orange and green lines in Fig. 5 (c). A similar behavior is observed for the negative value of  $H$ .

To compare the zero-field heating values of  $\rho_{xx}$  after FC in  $H = \pm 20$  kOe, we have plotted these values alongside the zero-field  $\rho_{xx}$  measured during heating without any cooling history in Fig. 5 (d). Surprisingly, these values almost overlap. To further support our claim,

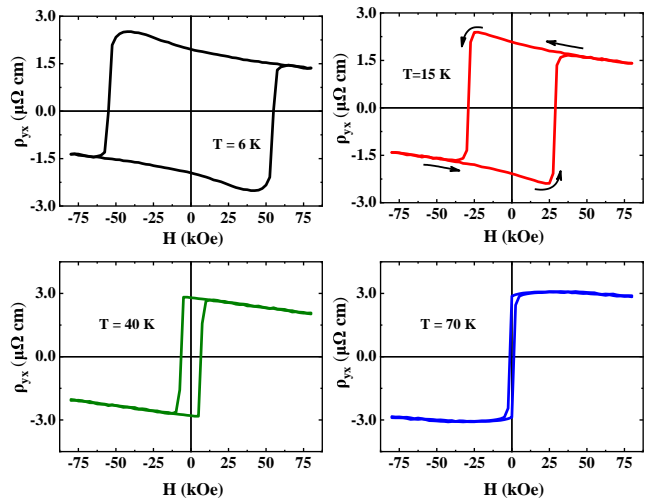


FIG. 6. Field variation of the Hall resistivity measured at different temperatures, after removing the MR contribution through anti-symmetrization.

we have plotted the thermoremanent magnetoresistance  $MR^{tr}$  versus  $T$  in the inset of Fig. 5(d), which shows nearly zero values at low  $T$ , indicating a negligible effect of TRM on  $\rho_{xx}$  within the resolution of our experiment. This observation is important for the subsequent sections.

The Hall resistivity ( $\rho_{yx}$ ) is measured in the Hall bar geometry by applying  $H$  along the  $c$  axis and an electric current in the  $ab$  plane. The variation of  $\rho_{yx}$  with  $H$  up to  $\pm 80$  kOe at different temperatures is shown in Fig. 6. In Hall measurement, a slight misalignment of the voltage leads can give rise to unwanted contributions from MR. To eliminate the MR contribution, we have anti-symmetrized  $\rho_{yx}$  for positive and negative values of  $H$ . The  $\rho_{yx}$  is found to be highly non-linear and exhibits a large hysteresis loop similar to the magnetization ( $M$ - $H$ ) curve, indicating contributions from the AHE.

For FM materials,  $\rho_{yx}$  is generally expressed by the following equation:

$$\rho_{yx} = \rho_{yx}^{OHE} + \rho_{yx}^{AHE} \quad (1)$$

where  $\rho_{yx}^{OHE}$  is the ordinary Hall effect, which arises due to the lateral motion of electrons due to the Lorentz force in a magnetic field, and  $\rho_{yx}^{AHE}$  is the anomalous Hall effect, which has a magnetic origin.

As shown in Fig. 6, the width of the hysteresis loop in  $\rho_{yx}$  decreases as  $T$  increases. On the other hand, the saturation value of  $\rho_{yx}$  increases with  $T$ . To estimate  $\rho_{yx}^{AHE}$  from the measured  $\rho_{yx}$ , we employed two different methods. In the first method, we measured the vertical width of  $\rho_{yx}$  at a particular temperature at the intercept with the  $H = 0$  axis, giving rise to  $2\rho_{yx}^{AHE}$ . In the second method, we linearly fitted the high-field saturated part of  $\rho_{yx}$  with respect to  $T$  and obtained  $\rho_{yx}^{AHE}$  from the

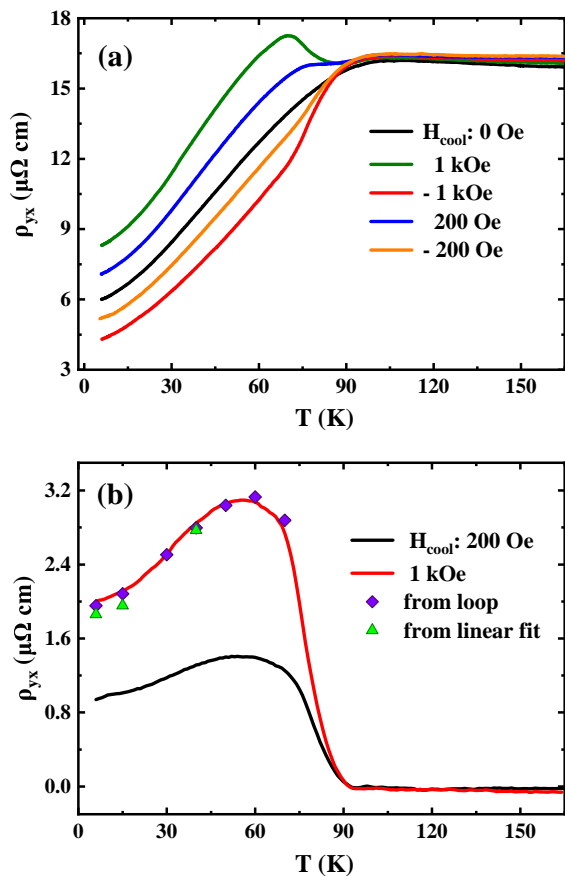


FIG. 7. (a) The sample is cooled under different positive and negative fields, referred to as  $H_{cool}$ . After reaching the lowest temperature (4 K), the field is removed, and  $\rho_{yx}$  is measured while heating the sample from 4 K. (b) Represents the variation of Hall resistivity after anti-symmetrization at different  $H_{cool}$  values. The symbols (diamond and triangle) show the values of  $\rho_{yx}$  obtained from the field variation of  $\rho_{yx}$  shown in Fig. 6.

intercept. The values obtained for  $\rho_{yx}^{AHE}$  are shown in Fig. 7 (b) purple diamond and green triangle symbols.

The most interesting observation of the study is the effect of TRM in  $\rho_{yx}$ . To understand this, we have cooled the sample from 180 to 4 K under different applied fields. After reaching 4 K, we set  $H$  at zero and measured  $\rho_{yx}$  while heating the sample. We call this thermoremanent Hall (TRH) resistivity ( $\rho_{yx}^{tr}$ ). The  $T$  variation of  $\rho_{yx}^{tr}$  in different cooling fields is shown in Fig. 7 (a). To remove the longitudinal resistivity contribution coming from voltage probe misalignment, we anti-symmetrize the data using the Hall resistivity measured for both positive and negative values of  $H$ , namely,  $\rho_{yx} = \frac{1}{2}[\rho_{yx}(+H) - \rho_{yx}(-H)]$  [27, 28]. The  $T$  variation of the symmetrized  $\rho_{yx}^{tr}$  is illustrated in Fig. 7 (b). It increases with increasing  $T$  and shows a maximum around 57 K then plunges to almost zero above 90 K. Interestingly, the value of  $\rho_{yx}^{tr}$  also depends on the cooling field. The black line in Fig. 7 (b) is taken, when the applied

cooling field was 200 Oe, slightly less to lock the system in the arrested state. On the other hand, the 1 kOe cooling field is sufficient to lock the system in the saturation magnetization state. We compared  $\rho_{yx}^{tr}$  with the  $\rho_{yx}^{AHE}$  obtained from our  $\rho_{yx}$  versus  $H$  isotherms [Fig. 6] recorded at various  $T$ . As depicted in Fig. 7 (b),  $\rho_{yx}^{tr}$  and  $\rho_{yx}^{AHE}$  (as shown by the purple diamond and green triangle symbols) match surprisingly well. This indicates that the Hall resistivity measured in zero-field after suitable field cooling ( $H_{cool} \geq 500$  Oe) is actually the anomalous Hall resistivity, *i.e.*,  $\rho_{yx}^{tr} \equiv \rho_{yx}^{AHE}$ .

To further confirm that the  $T$  variation of  $\rho_{yx}$  is arising solely from the TRM, we have cooled the sample at a higher field (5 kOe) and measured the  $\rho_{yx}$  under a zero-field while heating. The  $T$ -variation retraces the exact same curve as 1 kOe. On the other hand, similar measurement on MR shows no effect in  $\rho_{xx}$ , *i.e.* TRM has no effect in  $\rho_{xx}$ . This establishes that  $\rho_{yx}$  is due to TRM in the system. This is a direct proof of the magnetic origin of the AHE present in the system.

To shed more light on the intercorrelation between  $\rho_{xx}$  and  $M$  with  $\rho_{yx}$ , we have plotted the  $T$  variation of  $M$  (green line),  $\rho_{xx}$  (red line) and  $\rho_{yx}$  (blue line) while heating after a FC with  $H_{cool} \geq 500$  Oe, designated as  $M^{tr}$ ,  $\rho_{xx}$  (after symmetrization) and  $\rho_{yx}^{tr}$  (after anti-symmetrization) respectively in Fig. 8 (a). Since  $\rho_{yx}^{tr}$  and  $\rho_{yx}^{AHE}$  are equivalent to each other, the anomalous Hall resistivity often described as,

$$\rho_{yx}^{tr} = \alpha\rho_{xx} + \beta\rho_{xx}^2 \quad (2)$$

The variation of  $\rho_{yx}^{tr}$  with  $\rho_{xx}$  is plotted in Fig. 8 (b). The solid red line represents the fit to the data using eqn. 2. The fitting model converges for  $\alpha = 9.46 \times 10^{-3}$  and  $\beta = 1.86 \times 10^{-5} (\mu\Omega\text{-cm})^{-1}$ . This suggests that  $\rho_{yx}^{tr}$  is dominated by an extrinsic skew scattering mechanism.

To investigate the effect of TRM on  $\rho_{yx}^{tr}$ , we have employed the following mathematical expression (see eqn. 3), which establishes a connection between the two quantities when no external magnetic field ( $H$ ) is applied [29].

$$\rho_{yx}^{tr} = S_H M^{tr} \rho_{xx}^2 \left(1 + \frac{\alpha'}{\rho_{xx}}\right) \quad (3)$$

Here,  $S_H$  and  $\alpha'$  serve as fitting parameters. Fig. 8 (c) presents the plot of  $\rho_{yx}^{tr} / M^{tr}$  against  $\rho_{xx}$ , with the data modeled using eqn. 3. The fitted curve closely matches the experimental trend, revealing a coupled variation between TRH and TRM. The values of the extracted parameter from the fitting are  $S_H = 0.022 \text{ V}^{-1}$  and  $\alpha' = 1.46 \times 10^{-6} (\Omega\cdot\text{m})$ , highlighting the consistency of the model with the observed data.

#### IV. DISCUSSIONS

The structural analysis confirms that  $\text{Fe}_x\text{TaS}_2$  adopts a hexagonal crystal structure with the  $P6_3/mmc$  space

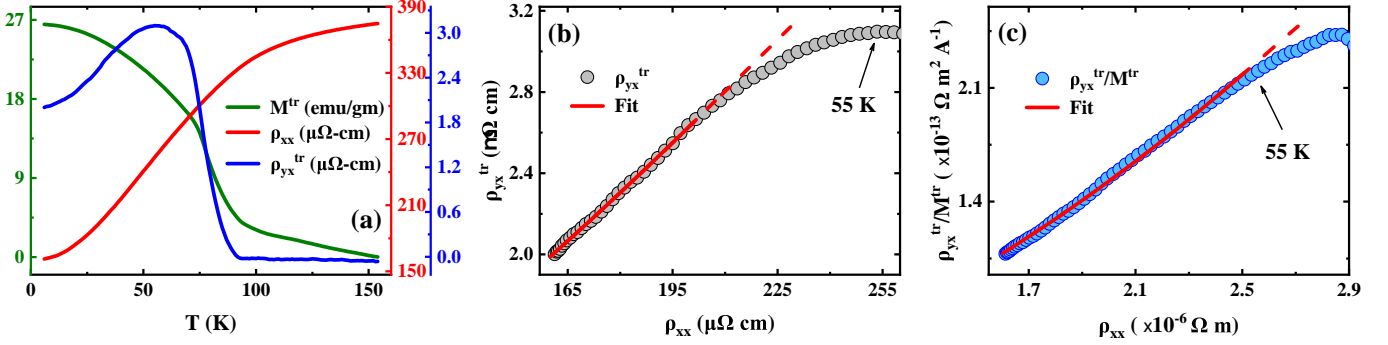


FIG. 8. (a)  $T$  variation of the magnetization, longitudinal resistivity and Hall resistivity obtained during zero-field heating after a FC with  $H_{cool} \geq 500$  Oe. The superscript 'tr' represents thermoremanent as these quantities are originating due to TRM. (b) Plot of  $\rho_{yx}^{tr}$  with the variation of  $\rho_{xx}$ . The red line represents the fitting using eqn. 2 in the low  $T$  region. (c) The variation of  $\rho_{yx}^{tr}/M^{tr}$  with longitudinal resistivity without any cooling history ( $\rho_{xx}$ ). The solid red line displays the fit using eqn. 3.

group, closely resembling the structure of its  $\text{Fe}_{1/4}\text{TaS}_2$  counterpart [30]. This similarity is strongly supported by SEM-EDX analysis, which indicates an Fe content of approximately 0.27, consistent with the stoichiometry of  $\text{Fe}_{1/4}\text{TaS}_2$ .

$\text{Fe}_x\text{TaS}_2$  is an Ising ferromagnet showing a large coercive field and a sharp magnetization reversal. The uniaxial magnetic anisotropy is prevalent in the sample, with the crystallographic  $c$  axis being the easy axis of magnetization. Most interestingly, the sample shows a large TRM, when it is cooled under a field greater than 500 Oe. On heating in a zero-field, the TRM diminishes and eventually vanishes above 160 K. The TRM also gives rise to AHE in zero applied field, which is found to be non-zero up to about 90 K.

Such TRM effects are quite common in glassy magnetic systems, where the disordered spin configuration and frustration lead to metastable states that retain the memory of the applied field [24]. However, in the present system, the absence of a glassy magnetic ground state is evident from our field-cooled-field-stop memory measurements. This suggests that the TRM effect in this material is driven by a fundamentally different mechanism compared to conventional glassy systems.

There are instances in single crystalline ferro or ferri-magnetic samples without glassy nature, where TRM is observed. For example, TRM is observed in  $\text{YFeO}_3$ ,  $\text{EuS}$ ,  $\text{FeS}_{1.14}$  (pyrrhotite), and it is associated with a strong magneto-crystalline anisotropy [31]. Our  $\text{Fe}_x\text{TaS}_2$  also belongs to this category, where we observe TRM in the absence of apparent disorder or glassiness.

The mechanism of TRM in our single-crystalline sample can be understood from the nature of the Ising spins. Close to the Curie-point, the magnetic anisotropy is weak, and cooling in a positive field ( $H_{cool} \parallel c$ ) from well above  $T_C$  down to 3 K, will produce a single-domain state with all the spin directed along the easy axis. On removing the field at 3 K, the spins will still remain aligned because the anisotropy energy is high at low temperature.

In the Landau-type free energy scenario, there exists a potential barrier between the up spins ( $\uparrow$ ) and the down spins ( $\downarrow$ ). On heating the sample in zero-field with the field-cooling history, the sample does not get demagnetized immediately because of the presence of this free energy barrier. The demagnetization is further restricted, as it is energetically unfavorable to have domains with spins along the hard axis. As we continue to heat the sample, there can be  $\uparrow \rightarrow \downarrow$  switching assisted by thermal energy. Furthermore, the anisotropy energy decreases, enabling the system to have domains in all possible directions, and eventually the TRM value drops significantly when heated above  $T_C$ . It is interesting to note that a small but finite TRM still continues to exist even at a temperature as high as 160 K. This TRM above  $T_C$  can be attributed to the presence of a short-range correlation in the sample. However, thermo-remanent Hall vanishes exactly at  $T_C$ , which possibly indicates that AHE ceased to exist in absence of a true long-range magnetically ordered state.

The Hall voltage observed in the zero-field heating path after being field cooled is associated with the TRM of the sample. This is evident from the linear nature of the  $\rho_{yx}^{tr}/M^{tr}$  vs.  $\rho_{xx}$  plot at least below 55 K. We find that  $\rho_{yx}^{tr}$  is primarily dominated by the extrinsic skew scattering mechanism.

In conclusion, observe large thermoremanence in  $M$  and  $\rho_{yx}$ , when the sample is cooled in a moderate field from  $T > T_C$ . The thermoremanence slowly decreases when heated in zero-field, and eventually vanishes above  $T_C$ . It should be noted that, unlike Hall, no thermoremanence is observed in the magnetoresistance data. The observed thermoremanence can be traced back to the strong magnetocrystalline anisotropy present in the sample.

## ACKNOWLEDGMENTS

MN would like to thank CSIR, India, for his research fellowship [File No. 09/080(1131)/2019-EMR-I]. The

UGC DAE-CSR Kolkata center of the UGC is acknowledged for providing the necessary facilities.

- 
- [1] L. Stojchevska, I. Vaskivskiy, T. Mertelj, P. Kusar, D. Svetin, S. Brazovskii, and D. Mihailovic, *Science* **344**, 177 (2014).
- [2] X. Lin, W. Yang, K. L. Wang, and W. Zhao, *Nature Electronics* **2**, 274 (2019).
- [3] S. Manzeli, D. Ovchinnikov, D. Pasquier, O. V. Yazyev, and A. Kis, *Nature Reviews Materials* **2**, 17033 (2017).
- [4] B. Sipos, A. F. Kusmartseva, A. Akrap, H. Berger, L. Forró, and E. Tutiš, *Nature Materials* **7**, 960 (2008).
- [5] F. D. S. J.A. Wilson and S. Mahajan, *Advances in Physics* **24**, 117 (1975).
- [6] R. E. Thomson, B. Burk, A. Zettl, and J. Clarke, *Phys. Rev. B* **49**, 16899 (1994).
- [7] M. Yoshida, Y. Zhang, J. Ye, R. Suzuki, Y. Imai, S. Kimura, A. Fujiwara, and Y. Iwasa, *Scientific Reports* **4**, 7302 (2014).
- [8] K. T. Law and P. A. Lee, *Proceedings of the National Academy of Sciences* **114**, 6996 (2017).
- [9] M. Klanjšek, A. Zorko, R. Žitko, J. Mravlje, Z. Jagličić, P. Biswas, P. Prelovšek, D. Mihailovic, and D. Arčon, *Nature Physics* **13**, 1130 (2017).
- [10] S. Mañas-Valero, B. M. Huddart, T. Lancaster, E. Coronado, and F. L. Pratt, *npj Quantum Materials* **6**, 69 (2021).
- [11] Y. Togawa, T. Koyama, K. Takayanagi, S. Mori, Y. Kousaka, J. Akimitsu, S. Nishihara, K. Inoue, A. S. Ovchinnikov, and J. Kishine, *Phys. Rev. Lett.* **108**, 107202 (2012).
- [12] D. A. Mayoh, J. Bouaziz, A. E. Hall, J. B. Staunton, M. R. Lees, and G. Balakrishnan, *Phys. Rev. Res.* **4**, 013134 (2022).
- [13] H. Takagi, R. Takagi, S. Minami, T. Nomoto, K. Ohishi, M.-T. Suzuki, Y. Yanagi, M. Hirayama, N. D. Khanh, K. Karube, H. Saito, D. Hashizume, R. Kiyonagi, Y. Tokura, R. Arita, T. Nakajima, and S. Seki, *Nature Physics* **19**, 961 (2023).
- [14] M. Eibschütz, S. Mahajan, F. J. DiSalvo, G. W. Hull, and J. V. Waszczak, *Journal of Applied Physics* **52**, 2098 (1981).
- [15] J. Dijkstra, P. J. Zijlema, C. F. van Bruggen, C. Haas, and R. A. de Groot, *Journal of Physics: Condensed Matter* **1**, 6363 (1989).
- [16] H. Narita, H. Ikuta, H. Hinode, T. Uchida, T. Ohtani, and M. Wakihara, *Journal of Solid State Chemistry* **108**, 148 (1994).
- [17] C.-W. Chen, S. Chikara, V. S. Zapf, and E. Morosan, *Phys. Rev. B* **94**, 054406 (2016).
- [18] J. G. Checkelsky, M. Lee, E. Morosan, R. J. Cava, and N. P. Ong, *Phys. Rev. B* **77**, 014433 (2008).
- [19] G. M. Sheldrick, *Acta Crystallographica Section A* **64**, 112 (2008).
- [20] V. Petříček, L. Palatinus, J. Plášil, and M. Dušek, *Zeitschrift für Kristallographie - Crystalline Materials* **238**, 271 (2023).
- [21] B. Huang, G. Clark, E. Navarro-Moratalla, D. R. Klein, R. Cheng, K. L. Seyler, D. Zhong, E. Schmidgall, M. A. McGuire, D. H. Cobden, W. Yao, D. Xiao, P. Jarillo-Herrero, and X. Xu, *Nature* **546**, 270 (2017).
- [22] R. V. Chamberlin, G. Mozurkewich, and R. Orbach, *Phys. Rev. Lett.* **52**, 867 (1984).
- [23] P. Nordblad, P. Svedlindh, L. Lundgren, and L. Sandlund, *Phys. Rev. B* **33**, 645 (1986).
- [24] J. Mydosh, *Spin Glasses: An Experimental Introduction* (Taylor & Francis, 1993).
- [25] R. Mathieu, P. Jönsson, D. N. H. Nam, and P. Nordblad, *Phys. Rev. B* **63**, 092401 (2001).
- [26] W. J. Hardy, C.-W. Chen, A. Marcinkova, H. Ji, J. Sinova, D. Natelson, and E. Morosan, *Phys. Rev. B* **91**, 054426 (2015).
- [27] Q. Wang, S. Sun, X. Zhang, F. Pang, and H. Lei, *Phys. Rev. B* **94**, 075135 (2016).
- [28] H. Li, B. Zhang, J. Liang, B. Ding, J. Chen, J. Shen, Z. Li, E. Liu, X. Xi, G. Wu, Y. Yao, H. Yang, and W. Wang, *Phys. Rev. B* **101**, 140409 (2020).
- [29] B. J. Chapman, M. G. Grossnickle, T. Wolf, and M. Lee, *Phys. Rev. B* **88**, 214406 (2013).
- [30] E. Morosan, H. W. Zandbergen, L. Li, M. Lee, J. G. Checkelsky, M. Heinrich, T. Siegrist, N. P. Ong, and R. J. Cava, *Phys. Rev. B* **75**, 104401 (2007).
- [31] Y. SYONO, S. AKIMOTO, and T. NAGATA, *Journal of geomagnetism and geoelectricity* **14**, 113 (1962).